Simultaneous dynamic optical and electrical properties of endothelial cell attachment on indium tin oxide bioelectrodes

Chang K. Choi
Anthony E. English
Kenneth D. Kihm
Charles H. Margraves
University of Tennessee
Department of Mechanical, Aerospace and Biomedical Engineering
Knoxville, Tennessee 37996

Abstract. This study quantifies the dynamic attachment and spreading of porcine pulmonary artery endothelial cells (PPAECs) on optically thin, indium tin oxide (ITO) biosensors using simultaneous differential interference contrast microscopy (DICM) and electrical microimpedance spectroscopy. A lock-in amplifier circuit monitored the impedance of PPAECs cultivated on the transparent ITO bioelectrodes as a function of frequency between 10 Hz and 100 kHz and as a function of time, while DICM images were simultaneously acquired. A digital image processing algorithm quantified the cell-covered electrode area as a function of time. The results of this study show that the fraction of the cell-covered electrode area is in qualitative agreement with the electrical impedance during the attachment phase following the cell settling on the electrode surface. The possibility of several distinctly different states of electrode coverage and cellular attachment giving rise to similar impedance signals is discussed. [DOI: 10.1117/1.2821407]

Keywords: biological cell; cell adhesion; differential interference contrast microscopy; endothelial; impedance; indium tin oxide; optical biosensor.

Paper 07096RR received Mar. 13, 2007; revised manuscript received Jun. 20, 2007; accepted for publication Jul. 5, 2007; published online Dec. 28, 2007.

1 Introduction

Simultaneously acquired optical microscopic images and electrical microimpedance measurements have a number of potential biomedical applications. Although the information obtained from microimpedance measurements complement many existing optical microscopy techniques, it is a complicated and sensitive function of the cellular state. In particular, the measured electrical impedance is a function of the cellular morphology, cell-matrix attachment, and the degree of cell-cell contacts. Combined optical and microimpedance measurements, therefore, have the potential to elucidate a number of complex cellular processes that optical and electrical measurements are not capable of independently.

A particularly novel approach to cellular impedance measurements was pioneered by Giaever and Keese.[1,2] Since then, electrical impedance measurements have been applied to a number of biological problems that deal with cellular barrier function and adhesion.[3–5] Electrical impedance measurements have been used to evaluate the model parameters associated with cell-cell and cell-matrix junction formation.[6,7] In addition, measurements at a single frequency have found applications in cellular motility studies. The vast majority of these studies, however, have been performed using gold microelectrode arrays. Although gold electrodes have attractive properties, they are relatively opaque, making simultaneous microscopy measurements difficult or infeasible in most cases.

Indium tin oxide (ITO) films have the unique property of being both electrically conductive and optically transparent.[8–10] As a result, ITO films have found a number of interesting applications in studying surface molecular biology[11,12] and excitable cells.[13–16] There have, however, been surprisingly few ITO applications in the measurement of cellular barrier function. Hillebrandt et al.[17] examined the thrombin-induced changes in human umbilical vein endothelial cell barrier function while acquiring phase contrast microscopy images. Choi et al.[18] examined the properties of an ITO silicon nitride electrode and its use to electrically measure the growth, attachment, and response of porcine endothelial cells to the drug Cytochalasin D. The results of these studies demonstrate the potential of ITO bioelectrodes for acquiring simultaneous optical and electrical measurements.

This study examines the time-dependent attachment and spreading of porcine pulmonary artery endothelial cells (PPAECs) on optically thin ITO electrodes using concurrent optical and electrical microimpedance measurements. Specifically, differential interference contrast microscopy (DICM) images are recorded simultaneously with frequency-dependent resistance and reactance measurements as a function of time. By digitally processing the images, the time-dependent changes in cellular morphology and electrode coverage are obtained and compared with the corresponding impedance measurements.

Address all correspondence to Anthony E. English, 308 Perkins Hall, University of Tennessee, Knoxville, TN 37996. Tel: 865-974-8392, Fax: 865-974-7663; E-mail: tenglish@utk.edu

1083-3668/2007/12(6)/064028/8/$25.00 © 2007 SPIE

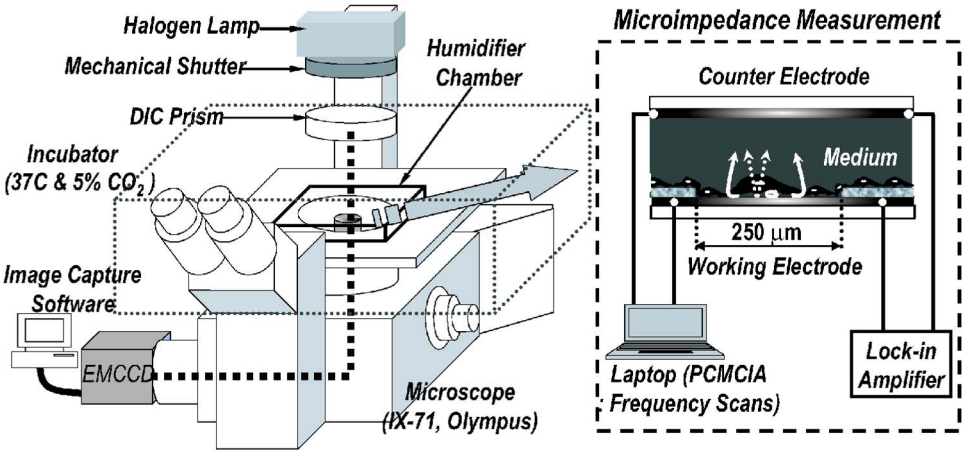

Fig. 1 Integrated optical and electrical impedance measurement system schematic. DICM images are acquired simultaneously with electrical impedance measurements. An environmental chamber maintains a humidified, 37 °C, and 5% CO_2 atmosphere for dynamic long time-lapse measurements. The measured impedance is a function of the current flow under the cells, between the cells, and the capacitively coupled current through the cell membranes.

2 Methods and Materials

2.1 *Microscopy and Image Processing*

Figure 1 shows a schematic of the optical and electrical impedance measuring apparatus. A SR830 lock-in amplifier (Stanford Research Systems, Sunnyvale, California) circuit generated a current through the ITO electrode and measured the resulting electrode voltage. A computer equipped with a Personal Computer Memory Card International Association card and a LABVIEW-based data acquisition program controlled the amplifier and performed frequency scans. Cells were kept viable using an incubator (WeatherStation, Olympus, Center Valley, Pennsylvania) that kept the temperature (37 °C), humidity, and CO_2 (5%) levels constant. These controlled conditions were crucial to keep cells alive during long time-lapse measurements. The imaging system consisted of a 20×-long working distance objective lens with a numerical aperture (NA) equal to 0.4, an Olympus model IX-71 inverted microscope with a polarizer (IX-LWPO), a DIC prism (IX2-DIC20) in the long working distance DIC condenser (IX2-LWUCD, NA=0.55), a transmitted Nomarski prism (U-DICTS), an analyzer (IX2-AN), a 100-W halogen lamp house (U-LH100-3, Olympus), and a Hamamatsu 14-bit electron multiplier (EM) cooled and intensified–charge-coupled device (CCD) digital camera. Additionally, a mechanical shutter was synchronized with the CCD camera to minimize any effects the halogen lamp may have had on cell growth.[19] The total magnification used in the current imaging system was 32×, resulting from a 20× objective lens and a 1.6× lens, which approximately fit the entire ITO working electrode. Differential interference contrast image and impedance measurements were taken simultaneously at 3-min time intervals.

Image processing was performed using a series of deconvolution and edge detection filters to identify the cell boundaries and to estimate the total cell-covered electrode area. Each image was deconvolved using a Lucy-Richardson deconvolution algorithm with a Gaussian point spread function, and the background was removed from the cell-covered areas using high and low threshold limits.[20] Binary images were obtained using Canny and Sobel filters. An overlay image was subsequently constructed to compare the digitally processed image with the original image. This permitted the cell-covered area to be quantified by determining the total number of pixels that had not been eliminated by the filters.

2.2 *Electrical Impedance Measurements*

Figure 2 shows a schematic of the impedance measuring circuit. Electrical impedance measurements were performed using a SR830 lock-in amplifier. A 1-V_{rms} ac signal was generated and connected to an electrode array via a 1-MΩ resistor. Although this provided an approximately 1-μA current source, corrections based on the circuit model were made to estimate the actual impedance from the electrode voltage measurement. The lock-in amplifier had an input impedance characterized by a parallel combination of a 10-MΩ resistor

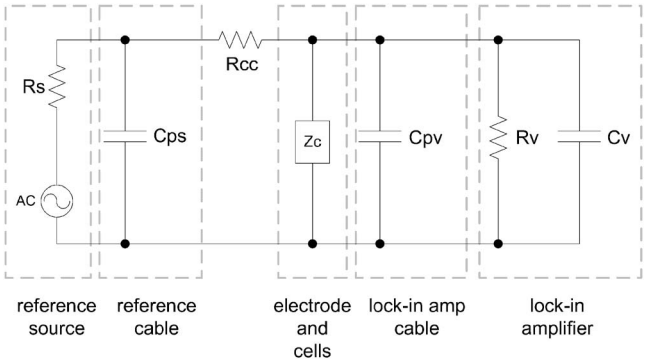

Fig. 2 Impedance measuring circuit configuration schematic. A 1-V ac signal is applied to an electrode via a 1-MΩ resistor, R_{cc}. The source resistance, R_s, is 50 Ω and the input impedance to the lock-in amplifier is equivalent to a parallel combination of a 10-MΩ resistor and 25-pF capacitor. The reference cable coaxial leads and lock-in amplifier coaxial leads introduce into the circuit parallel capacitances C_{ps} and C_{pv}, respectively. The electrode impedance, Z_c, is estimated by voltage measurements and a voltage-to-impedance conversion based on this circuit.

and a 25-pF capacitor. The ac voltage source resistance was 50 Ω, and the capacitance of each coaxial lead, C_{pv} and C_{ps}, was approximately 86 pF. Fabrication of the ITO electrodes is explained in detail in Choi et al.[18]

The voltage was sampled at a rate of 32 samples per second using a filter time constant of 32 ms and a 12-dB/decade roll-off every 3 min. The averages and standard deviations of the 32 sampled voltages were calculated for each set of measurements. Frequency sweeps using 15 logarithmically spaced frequency samples between 10 Hz and 100 kHz were obtained for the naked electrode and the cell-inoculated electrode during cellular attachment.

2.3 *Cell Culture*

PPAECs were isolated from fresh porcine arteries obtained from a local abattoir. The endothelial cells were removed from the intimal artery walls by carefully scraping them off with a scalpel. The cell culture media consisted of M199 (GibcoBRL, Baltimore, Maryland) and 10% fetal bovine serum (Hyclone, Logan, Utah) supplemented with basal medium eagle (BME) vitamins (Sigma-Aldrich, St. Louis, Missouri), L-glutamine (GibcoBRL), penicillin and streptomycin (GibcoBRL), and BME amino acids (Sigma). The culture was maintained until the cells reached confluence, and then they were passaged. Passaging generally occurred once a week, and passages 4 through 8 were used for testing in this study. Trypsin–ethylenediamine tetraacetic acid (1X, GibcoBRL) was used to detach cells for passaging and electrode inoculation. Cells were cultivated in an incubator that kept the temperature at 37 °C and the CO_2 level at 5%. Cells suspended in M199 were inoculated directly onto a sterilized ITO-Si_3N_4 microelectrode that was not previously coated with any adhesion molecules such as fibronectin. High and low cellular inoculation densities were chosen to produce either a subconfluent pattern or a confluent pattern following the initial attachment phase.

3 Results

3.1 *Electrical Scan Summary*

Figure 3 shows the time-dependent changes in normalized resistance and reactance at 1.0, 1.77, 3.16, and 5.62 kHz during the attachment of PPAECs to a 250-μm diameter ITO electrode. The zero time point corresponds to the cell inoculation time. The normalized resistance, $(R_c-R_n)/R_n$, and the normalized reactance, $(X_c-X_n)/X_n$, were calculated from the cell covered and naked electrode resistances, R_c and R_n, and reactances, X_c and X_n, respectively. An initial peak in the normalized resistance and reactance occurred approximately 4 h after cell inoculation on the ITO electrodes. Following the initial peak, the normalized resistance and reactance stabilized and slowly decreased over several hours. The normalized resistive component of the naked electrode was consistent with small amounts of drift. In addition, changes in both the resistive and reactive components were observed during the first several scans until the environmental chamber parameters, such as the CO_2 level, pH, and temperature stabilized.

Figure 4 summarizes the time-dependent evolution of the normalized resistance and reactance as a function of frequency. The normalized resistance peaked around 1 kHz, and

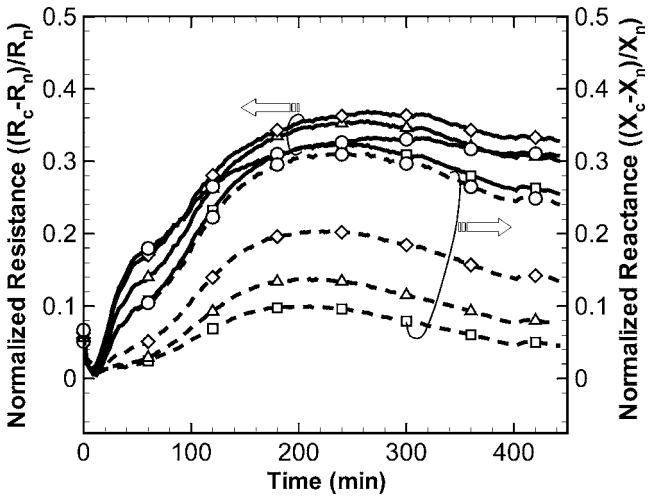

Fig. 3 Normalized resistances (solid lines) and normalized reactances (dashed-dotted lines) as a function of time. The terms *R* and *X* represent the resistance and reactance, respectively, and the subscripts *c* and *n* indicate cell-covered and naked scans, respectively. Among the 15 frequency scans acquired, 4 representative frequencies are selected to illustrate the cellular attachment of PPAECs to a 250-μm ITO electrode. For the sake of clarity, every 20th data point is marked with symbols: □ for 1.0 kHz, △ for 1.77 kHz, ◇ for 3.16 kHz, and ○ for 5.62 kHz.

the normalized reactance appeared to increase with increasing frequency following an initial attachment phase. The resistance and reactance changes were a complex function of the endothelial cell attachment, spreading, and micromotion. Although the impedance measurements were a sensitive function of the cellular attachment parameters, these measurements alone could not sufficiently evaluate the dynamic cellular morphology changes coupled to the cell-cell and cell-substrate adhesion, and cell-covered area on the working electrode.

3.2 *Image Segmentation and Cell-Covered Area Estimation*

Figure 5 shows a time series of endothelial cell DICM images of a 250-μm diameter ITO electrode following cellular inoculation densities that ultimately produced a subconfluent and confluent endothelial cell pattern. The first row shows the time series leading to a subconfluent pattern, and the second row shows the series leading to a confluent pattern. During the endothelial cell attachment and spreading process, the cells start with a globular morphology and then gradually flatten. For the case that produced a subconfluent pattern, approximately 25 cells became attached to the working electrode. Six minutes after inoculating the cells onto an ITO electrode, two cells began to spread, but the rest retained their globular morphology for approximately 30 to 33 min. In the case that produced a confluent pattern, approximately 6 min after inoculation, a few cells began spreading, but most cells remained globular for approximately 30 to 33 min. After this time, the cell-covered area remained almost constant. However, the cells became more tightly packed and much flatter over time. There were approximately 55 and 65 cells on the working electrode at $t=450$ min and $t=900$ min, respec-

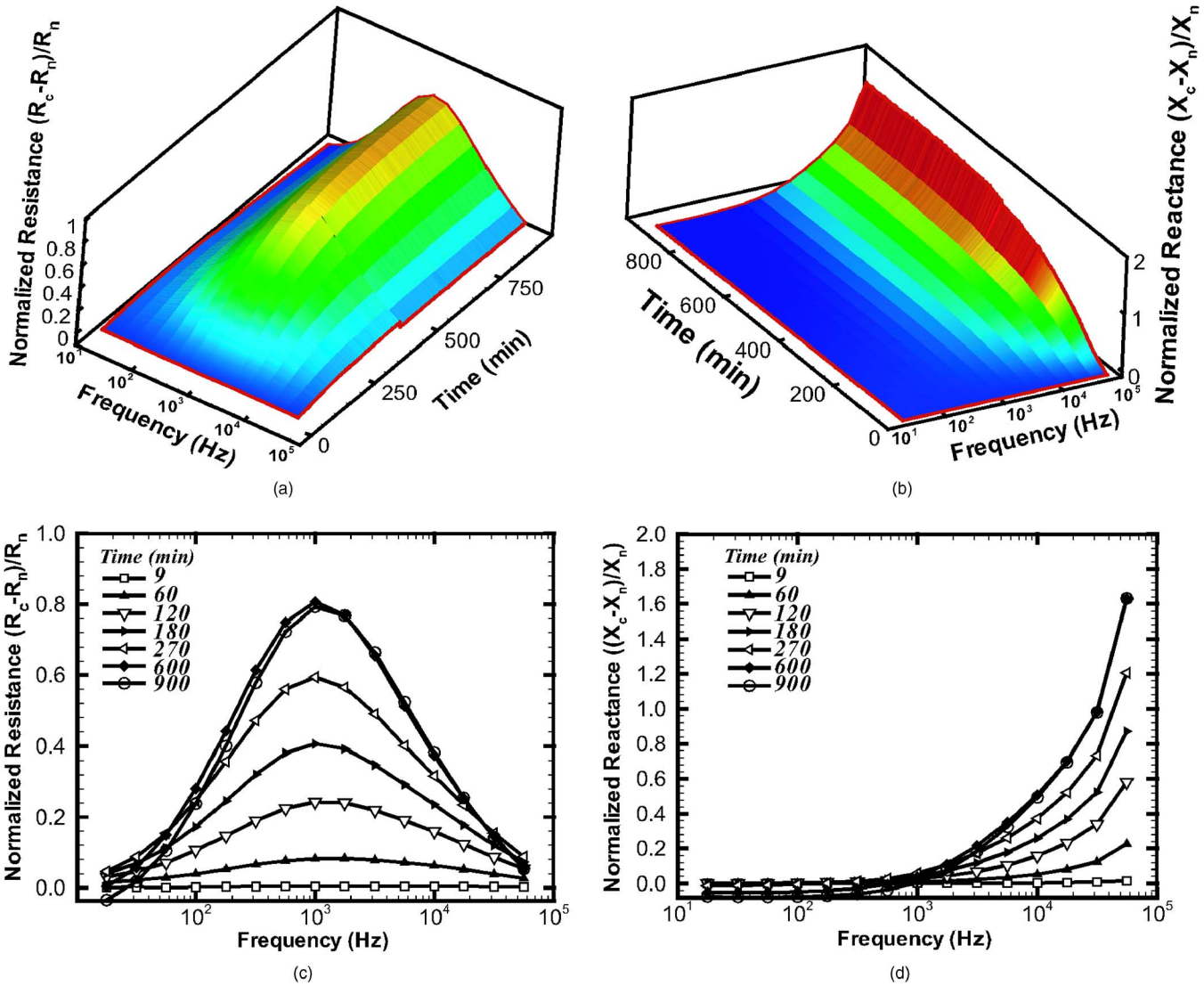

Fig. 4 Representative surface plots of normalized resistance (a) and reactance (b) attach scans of PPEACs on a 250-μm diameter ITO electrode as a function of frequency and time following a confluent inoculation density. The surfaces consist of approximately 300 frequency spectrum scans that were sampled at 3-m time intervals. Plots (c) and (d) show normalized resistance and reactance, respectively, for PPEACs's attachment at t =9, 60, 120, 180, 270, 600, and 900 min. (c) The normalized resistance as a function of frequency shows a monotonic increase with time up to approximately 600 min at which point saturation occurs. (d) The corresponding normalized reactance also shows an increase with time during the cellular attachment phase.

tively. For inoculations that produced subconfluent and confluent endothelial cell patterns, the time required for the initial cell spreading stayed relatively constant. Another comparison made for these two cases was the settling time, defined as the initial time when the number of cells remained constant for a period of four consecutive images. The settling time for the case that produced a confluent pattern was approximately 15 to 18 min, while the settling time for the case that produced a subconfluent pattern was approximately 21 to 27 min.

Figure 6 summarizes the image processing results used to evaluate the cell-covered electrode area in this study. A deconvolved image (a) was first obtained using a Gaussian point spread function. The following image (b) removed a portion of the background from the cell-covered areas using high and low threshold limits and a complete binary image (c) was separately obtained using a Canny or Sobel filter. The local gradients were compared to high and low threshold values, either provided by the user or internally calculated, to roughly detect the cell boundary. A pixel-by-pixel comparison of images (b) and (c) was then made to more accurately define the cell membrane boundaries. Generally, a portion of each cell was removed using the threshold filter because some of these pixels had similar intensities compared to those of the surrounding medium. This is a general characteristic of DICM. The intensities in a cell varied from darker to brighter or brighter to darker along the shear axis. The diagonal filter compensated for this eliminated area and specified single cells. Another filter, called a stitch filter, was employed to completely fill holes in cells to produce image (f). Finally, a removal filter deleted the defects that appeared as cells but were possibly small air bubbles or optical artifacts. The final

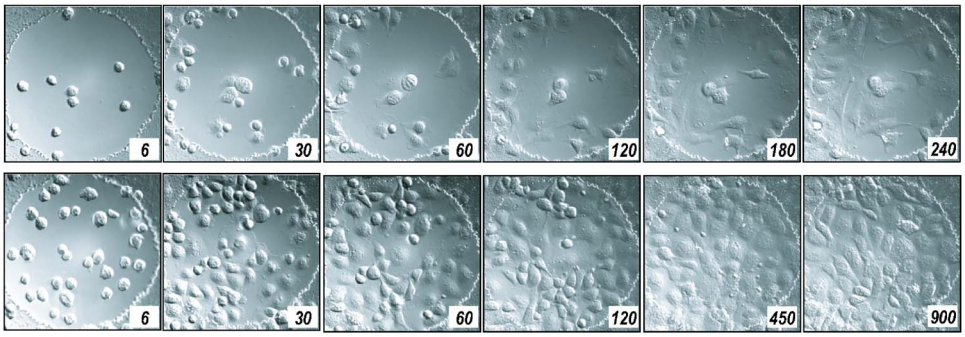

Fig. 5 DICM images of PPAECs on a 250-μm diameter ITO-Si_3N_4 electrode. The top row shows a set of images for a subconfluent inoculation, and the bottom row shows a set of images for a confluent inoculation. The magnification is 32× providing a 250-×-250-μm^2 field of view. The initial inoculation density was carefully chosen to produce either a subconfluent or confluent endothelial cell attachment pattern.

overlay image (h) was constructed from images (a) and (g) to compare the digitally processed image with the original image. The last image (h) shows the area covered by cells using the image processing algorithm and quantifies any eliminated or overestimated areas produced by the algorithm.

Figure 7 shows four digitally processed representative overlay images of PPAECs and the normalized cell-covered area as a function of time. The image processing software identified single cells and their boundaries until they reached confluence. Overlay images were used to visually check cell-occupied areas overestimated or discarded from digital image processing. The graph validates the results obtained by digital image processing by comparing them with those acquired by manual area estimation. The average difference between digital image processing and manual area estimation for each experiment was observed to be less than 5%.

3.3 *Combined Electro-Optic Analysis*

Figure 8 compares the time-dependent changes in the normalized resistance and normalized cell-covered area for a subconfluent and confluent cell inoculation. In both cases, the normalized resistance did not completely reflect the amount of the electrode covered with cells. Changes in cell-matrix and cell-cell attachment, which altered the resistance, complicated the correlation between cell-covered area and resistance. In both cases, however, their time-dependent patterns are similar.

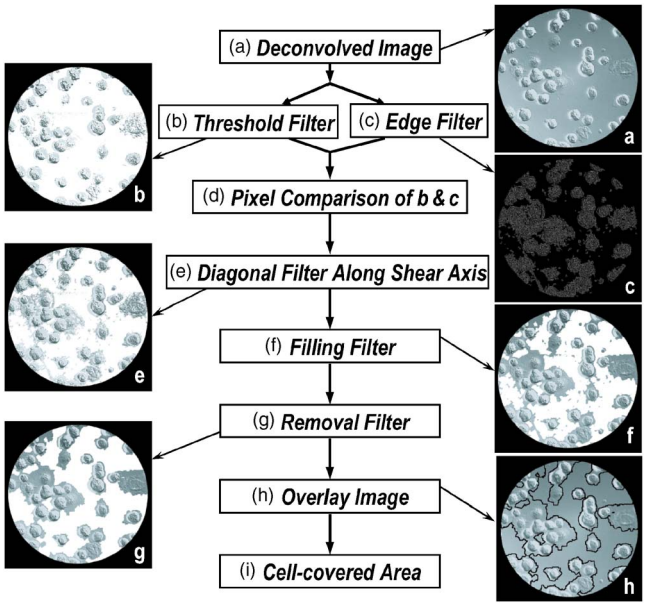

Fig. 6 Image processing flow chart and digitally processed images following each filter step. To automate the cell-covered area estimation, a sequence of image processing steps is carried out. (a) Deconvolved image with examined area outside electrode set to 0. (b) Image after applying threshold filtering with high and low threshold limits. (c) Binary image created using a Canny filter. (d) Pixel comparison step of images (b) and (c). (e) Image after applying diagonal filter along the shear axis. (f) Image after the filling filter. (g) Image after removal filter. (h) Overlaying image with (a) and (g) for the comparison of actual and calculated areas.

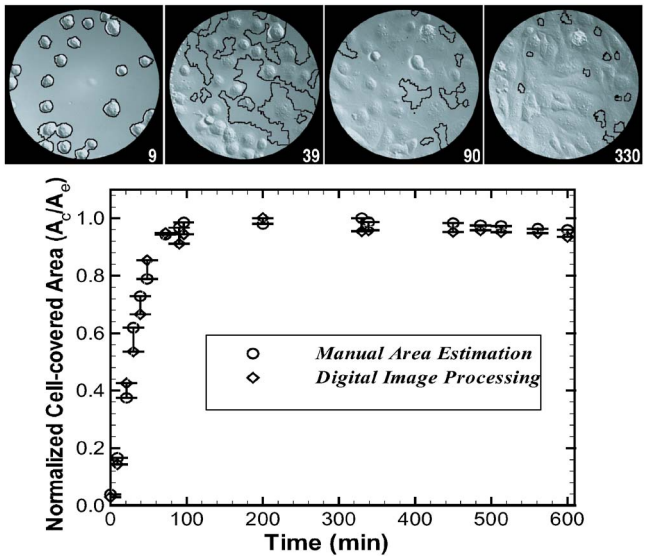

Fig. 7 Overlay images comparing the cell-covered areas estimated using the image processing algorithm and manual cell-covered area estimates. The overlay images are used to visually check the areas that are discarded or overestimated after image processing. The graph validates the cell-covered area estimates obtained from digital image processing by comparing those obtained by manually tracing the cell boundaries. The maximum difference between the two methods is approximately 8% for this sample where cells reached confluence at approximately 100 min. The term A_c denotes the cell-covered area and A_e denotes 0.043-mm^2 electrode area.

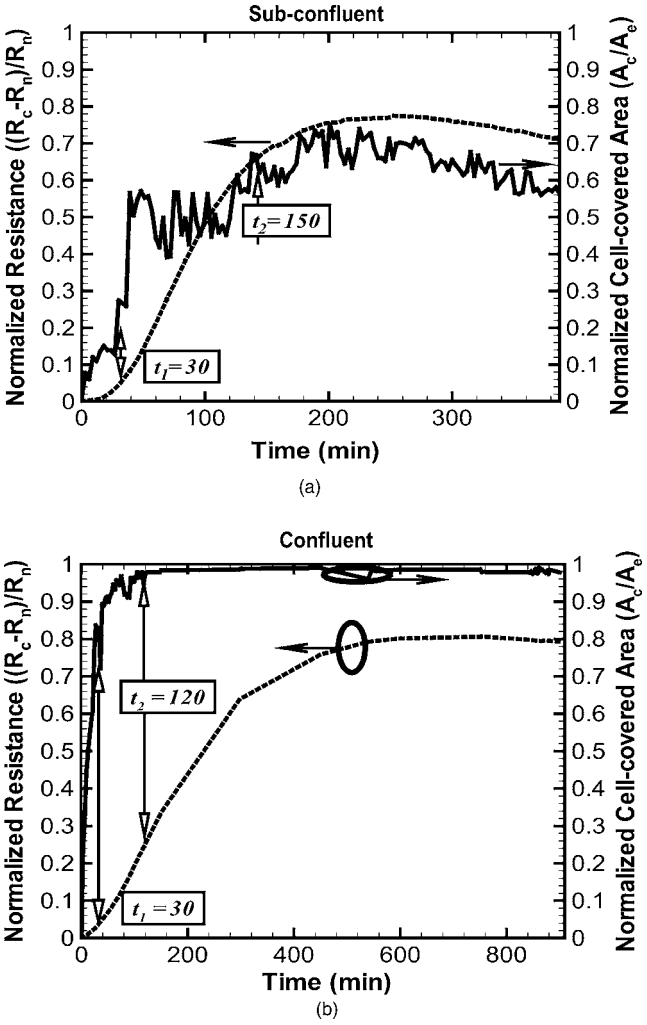

Fig. 8 Normalized resistance (dashed lines) and normalized cell-covered area (solid lines) vs time for the (a) subconfluent and (b) confluent cases shown in Fig. 5. The normalized resistance and the normalized cell-covered area have similar time-dependent patterns. Both electrical impedance and DICM image data were simultaneously acquired at 3-min time intervals.

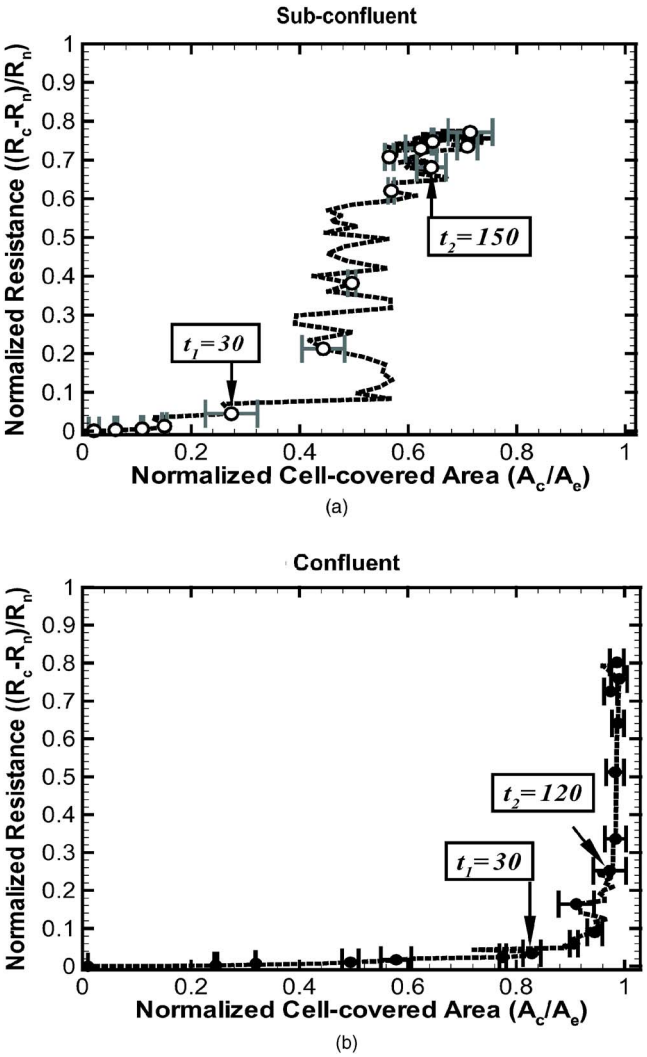

Fig. 9 Normalized resistance vs normalized cell-covered area for the (a) subconfluent and (b) confluent cases shown in Fig. 5. The error bars shown for selected data points indicate the difference between manual area estimates and those calculated using the digital image processing algorithm. Estimated errors for the normalized resistance are smaller than the symbol size. t_1 and t_2 represent the times necessary for most cells to spread and the time to reach approximately 5% of their maximum electrode covered area, respectively. For the confluent case, the maximum covered area is approximately 99% of the total electrode surface area, and for the subconfluent case, the maximum covered area is approximately 70% of the total electrode area.

Figure 9 illustrates the changes in normalized resistance with normalized cell-covered area for both the subconfluent and confluent cases. Three distinct intervals are considered and will be referred to as the settling zone, the linearly correlated zone, and the saturated zone. For the settling zone, the normalized cell-covered area first increases abruptly due to the increasing number of cells. A total of 25 cells in the subconfluent case and 65 cells in the confluent case do not appreciably change the normalized resistance. In the linearly correlated zone, the normalized cell-covered area proportionally increases with the normalized resistance showing both subconfluent and confluent cases have an analogous starting time, which is around t_1. Also, a linear relationship between the normalized cell-covered area and normalized resistance is shown. For the saturated zone, in the subconfluent case, the normalized cell-covered area slightly decreases while the normalized resistance remains relatively constant as the cell-substrate adhesion is much tighter and flatter. In the confluent case, however, the normalized cell-covered area remains constant while the normalized resistance continuously increases as a possible result of increasing cell-substrate and cell-cell adhesion. The cells look much flatter and more tightly packed in these cases. Changes in normalized resistance and reactance are a complicated function of the normalized cell-covered area, cell-cell adhesion, and cell-substrate adhesion. All of these factors can be considered both optically and electrically with a transparent conductive ITO electrode. Increasing cell-cell and cell-matrix adhesion states, however, are consistent with the more tightly packed and flatter cell morphologies. This confirms cellular attachment with ITO silicon nitride bioelectrodes as well as demonstrates that the

ITO electrode is a good tool for both electrical measurement and optical visualization.

Each subconfluent and confluent cellular inoculation needs to be considered on a case-by-case basis. For the confluent case, which lasted up to 19 h, the cell-covered electrode morphology is relatively constant after reaching confluence. However, the population of cells was observed to fluctuate. In another confluent case considered in this study, after 13 h some of the cells appeared to migrate from the working electrode surface to the insulating layer area thus leaving bare areas. In all the subconfluent cases, the cells migrate more freely than the confluent case, and as a result, there are greater fluctuations in the total cell-covered area.

4 Discussion

Although electrical signals are extremely sensitive to the different stages of cellular attachment, they are a complicated function of the degree of cell-cell and cell-matrix interaction as well as the fraction of the covered electrode surface area. Several degenerate states, giving similar electrical impedances, can potentially arise under very different degrees of electrode coverage and states of cellular attachment. In some cases, for example, it is possible to have a small fraction of the electrode covered by tightly adhering cells that gives rise to a similar impedance measurement produced by a confluent covering of loosely attached cells. Simultaneous optical images can provide a direct measure of the fraction of the electrode covered by cells and, therefore, remove this ambiguity.

The results of this study show that even when the electrode is inoculated with a large density of cells, a finite attachment time is required for cells to completely cover the electrode surface. During this time, it is easy to misinterpret the increasing electrical impedance signal as arising from the increasing degrees of cell-substrate or cell-cell attachment. A direct visual measurement will differentiate these states.

Different normalized resistance values were found for different tests due to several variables. First, the medium for each test may have a slightly different ion concentration. Second, the number of cells on the working electrode, as mentioned previously, varies with each test. Finally, the electrical characteristics of individual electrodes may change slightly over time. Therefore, the impedance values measured with different electrodes and at different times are not appropriate to directly compare with each other. As a result, a more accurate way to examine the effect of cell growth on the change in resistance over time is to supplement the resistance measurements with microscopic images.

The ability to simultaneously perform electrical impedance and optical imaging of cellular cultures has a number of potential applications. Microscopic images permit a more direct picture of cell-cell and cell-matrix states to be interpreted from electrical impedance measurements. The potential application of fluorescent molecules, particularly green fluorescent proteins, offer a number of opportunities for a more quantitative interpretation of electrical impedance measurements. The combination of interference reflection microscopy and electrical impedance measurements may further elucidate the role of cell-matrix adhesion on the electrical signal. In particular, interference reflection microscopy may help to quantify the role that cell-matrix separation distance fluctuations play in the measured impedance signal.

Excellent resolution and improved cell boundary visibility can be obtained using DICM, particularly in the adjoining cellular regions that have larger optical gradients. In general, the use of a high NA objective lens provides optical slicing in a thick specimen without confusing images. The shear axis, which is a chief characteristic in DICM and along which the maximum contrast exists, can be exploited in the application of image processing algorithms, particularly those that implement a diagonal filter. Annoying halos, encountered in phase contrast microscopy (PCM), are absent in DICM images. Plastic materials, such as tissue culture dishes, commercial gold electrodes, and other birefringent specimens, however, are not suitable for DICM measurements because of their affect upon polarized light. Thus, to properly use the DICM technique, all the materials along the light path must contain glass because plastics or acrylics change the characteristics of both the ordinary and extraordinary rays. The transparent conductive ITO-Si_3N_4 electrodes used in this experiment are sufficiently compatible with DICM imaging.

PCM yields image intensity values as a function of specimen optical path length magnitude, however, DICM creates the contrast by optical path length gradients, or the rate of change in the direction of wavefront shear. This is the most important characteristic that is exploited in the digital image processing. Unlike PCM, DICM produces an improved contrast image by introducing bias retardation by the objective Nomarski prism whose net result is to render the image in a pseudo three-dimensional relief, where regions of increasing optical path difference appear much brighter or darker.

The ITO electrodes used in this study were recyclable and, in fact, have been used more than 100 times so far without any apparent decrease in performance. Similar gold electrodes can typically be used only once. In addition, the ITO-Si_3N_4 electrodes were resistant to ethanol sterilization. Some forms of photoresist that are used for the insulating layer are solubilized in ethanol and are harder to sterilize and clean for repeated applications. Compared to silicon nitride, initial attempts to use SU-8 as a photoresist were unsuccessful because it was not resistant to ethanol sterilization. When the electrode arrays with an SU-8 photoresist were rinsed with ethanol, the SU-8 contracted or shrunk.

To effectively determine the settling time, and the spreading time, higher frame rates are strongly recommended. Additionally, higher frames per second are also needed to optically detect micromotion, motility, and cell-cell and cell-substrate interaction in detail. A single frequency scan for the impedance measurement of endothelial cells is desirable to electrically measure their sensitive activities.

5 Conclusion

The simultaneous dynamic optoelectric observation of endothelial cells using DICM imaging and impedance measurements provided a clearer interpretation of the time-dependent changes associated with cellular attachment and spreading. The combination of optical and electrical methods, therefore, provided a more quantitative and qualitative assessment of dynamic cellular morphology changes, cell-cell and cell-substrate adhesion changes, and cell-covered area changes.

The fraction of the cell-covered area was in qualitative agreement with the electrical impedance during the attachment phase following cells settling to the electrode surface. Digital image processing automated the cell-covered area estimation and was validated using manual area estimation.

Acknowledgments

This work was supported in part by a National Science Foundation Career Award No. BES-0238905 (AEE), by the Korea Institute of Science and Technology Evaluation Policy (KDK), and in part by an American Heart Association Grant No. 0265029B (AEE). The authors would like to thank Seung-Ik Jun and Philip D. Rack for their help with fabricating the ITO electrodes.

References

1. I. Giaever and C. R. Keese, "Monitoring fibroblast behavior in tissue culture with an applied electric field," *Proc. Natl. Acad. Sci. U.S.A.* **81**(12), 3761–3764 (1984).
2. I. Giaever and C. R. Keese, "Micromotion of mammalian cells measured electrically," *Proc. Natl. Acad. Sci. U.S.A.* **88**(17), 7896–7900 (1991).
3. A. R. Burns, R. A. Bowden, S. D. MacDonell, D. C. Walker, T. O. Odebunmi, E. M. Donnachie, S. I. Simon, M. L. Entman, and C. W. Smith, "Analysis of tight junctions during neutrophil transendothelial migration," *J. Cell. Sci.* **113**(1), 45–57 (2000).
4. A. R. Burns, D. C. Walker, E. S. Brown, L. T. Thurmon, R. A. Bowden, C. R. Keese, S. I. Simon, M. L. Entman, and C. W. Smith, "Neutrophil transendothelial migration is independent of tight junctions and occurs preferentially at tricellular corners," *J. Immunol.* **159**(6), 2893–2903 (1997).
5. J. Wegener, C. R. Keese, and I. Giaever, "Electric cell-substrate impedance sensing (ecis) as a noninvasive means to monitor the kinetics of cell spreading to artificial surfaces," *Exp. Cell Res.* **259**(1), 158–166 (2000).
6. A. E. English, J. C. Squire, J. E. Bodmer, and A. B. Moy, "Endothelial cell electrical impedance parameter artifacts produced by a gold electrode and phase sensitive detection," *IEEE Trans. Biomed. Eng.* **54**(5), 863–873 (2007).
7. A. E. English, C. P. Plaut, and A. B. Moy, "A Riemannian manifold analysis of endothelial cell monolayer impedance parameter precision," *J. Math. Biol.* **55**(5), 721–743 (2007).
8. S. Ray, R. Banerjee, N. Basu, A. K. Batabyal, and A. K. Barua, "Properties of tin doped indium oxide thin films prepared by magnetron sputtering," *J. Appl. Phys.* **54**(6), 3497 (1983).
9. S.-I. Jun, T. E. McKnight, M. L. Simpson, and P. D. Rack, "A statistical parameter study of indium tin oxide thin films deposited by radio-frequency sputtering," *Thin Solid Films* **476**(1), 59–64 (2005).
10. M. Penza, S. Cozzi, M. A. Tagliente, L. Mirenghi, C. Martucci, and A. Quirini, "Characterization of transparent and conductive electrodes of indium tin oxide thin films by sequential reactive evaporation," *Thin Solid Films* **349**(1), 71–77 (1999).
11. H. Hillebrandt, G. Wiegand, M. Tanaka, and E. Sackmann, "High electric resistance polymer/lipid composite films on indium-tin-oxide electrodes," *Langmuir* **15**(24), 8451–8459 (1999).
12. S. Gritsch, P. Nollert, F. Jahnig, and E. Sackmann, "Impedance spectroscopy of porin and gramicidin pores reconstituted into supported lipid bilayers on indium-tin oxide electrodes," *Langmuir* **14**(11), 3118–3125 (1998).
13. G. W. Gross, W. Y. Wen, and J. W. Lin, "Transparent indium-tin oxide electrodes patterns for extracellular, multisite recording in-neutronal cultures," *J. Neurosci. Methods* **15**(3), 243–252 (1985).
14. G. W. Gross, B. K. Rhoades, D. L. Reust, and F. U. Schwalm, "Stimulation of monolayer networks in culture through thin-film indium-tin oxide recording electrodes," *J. Neurosci. Methods* **50**(2), 131–143 (1993).
15. V. Bucher, B. Brunner, C. Leibrock, M. Schubert, and W. Nisch, "Electrical properties of a light-addressable microelectrode chip with high electrode density for extracellular stimulation and recroding of excitable cells," *Biosens. Bioelectron.* **16**(3), 205–210 (2001).
16. V. Bucher, M. Schubert, D. Kern, and W. Nisch, "Light-addressed sub-micron electrodes for extracellular recording and stimulation of excitable cells," *Microelectron. Eng.* **57**(1), 705–712 (2001).
17. H. Hillebrandt, A. Abdelghani, C. Abdelghani-Jaquin, M. Aepfelbacher, and E. Sackmann, "Electrical and optical characterization of thrombin-induced permeability of cultured endothelial cell monolayers on semiconductor electrode arrays," *Appl. Phys. A* **73**(5), 539–546 (2001).
18. C. K. Choi, A. E. English, S.-I. Jun, K. D. Khim, and P. D. Rack, "An endothelial cell compatible biosensor fabricated using optically thin indium tin oxide silicon nitride electrodes," *Biosens. Bioelectron.* **22**(11), 2585–2590 (2007).
19. C. K. Dorey, F. C. Delori, and K. Akeo, "Growth of cultured retinal pigment epithelial (rpe) and endothelial cell is inhibited by blue light but not green or red light," *Curr. Eye Res.* **9**(6), 549–559 (1990).
20. S. Venkataraman, J. L. Morrell-Falvey, M. J. Doktycz, and H. Qi, "Automated image analysis of fluorescence microscopic images to identify protein-protein interactions," in *Proceedings of the 2005 IEEE Engineering in Medicine and Biology 27th Annual Conference*, pp. 797–800 (2005).